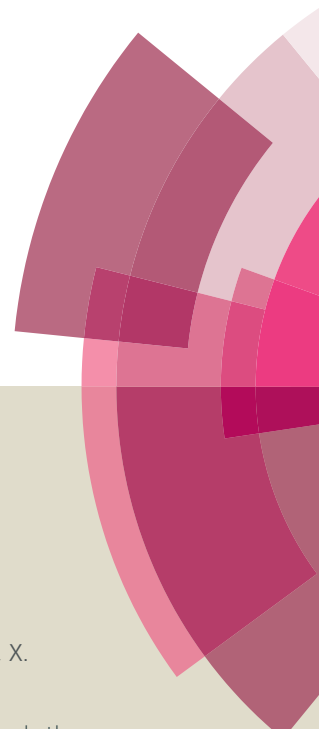


# Catalysis Science & Technology

Accepted Manuscript



This article can be cited before page numbers have been issued, to do this please use: H. Zhang, S. Qi, X. Niu, J. Hu, C. Ren, H. Chen and X. Chen, *Catal. Sci. Technol.*, 2014, DOI: 10.1039/C4CY00072B.



This is an *Accepted Manuscript*, which has been through the Royal Society of Chemistry peer review process and has been accepted for publication.

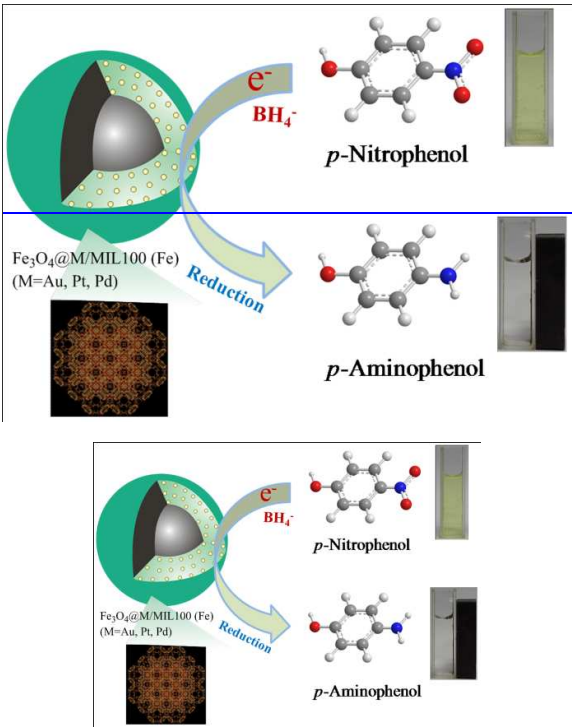
*Accepted Manuscripts* are published online shortly after acceptance, before technical editing, formatting and proof reading. Using this free service, authors can make their results available to the community, in citable form, before we publish the edited article. We will replace this *Accepted Manuscript* with the edited and formatted *Advance Article* as soon as it is available.

You can find more information about *Accepted Manuscripts* in the [Information for Authors](#).

Please note that technical editing may introduce minor changes to the text and/or graphics, which may alter content. The journal's standard [Terms & Conditions](#) and the [Ethical guidelines](#) still apply. In no event shall the Royal Society of Chemistry be held responsible for any errors or omissions in this *Accepted Manuscript* or any consequences arising from the use of any information it contains.

Graphical Abstract

Cauliflower-like porous magnetic MOFs embedded with noble metallic nanoparticles possesses superior catalytic performance and can be easily recycled.



**Metallic nanoparticles immobilized in magnetic metal-organic  
frameworks: preparation and application as highly active,  
magnetically isolable and reusable catalysts**

Hai-juan Zhang <sup>a</sup>, Sheng-da Qi <sup>a</sup>, Xiao-ying Niu <sup>a</sup>, Jing Hu <sup>a</sup>, Cui-ling Ren <sup>a</sup>, Hong-li  
Chen <sup>a</sup>, Xing-guo Chen <sup>a, b, \*</sup>

<sup>a</sup> *State Key Laboratory of Applied Organic Chemistry, College of Chemistry and  
Chemical Engineering, Lanzhou University, Lanzhou, Gansu 730000, China*

<sup>b</sup> *Key Laboratory of Nonferrous Metal Chemistry and Resources Utilization of Gansu  
Province, Lanzhou University, Lanzhou, Gansu 730000, China*

\* Corresponding author

E-mail address: [chenxg@lzu.edu.cn](mailto:chenxg@lzu.edu.cn)

Tel: 86-931-8912763

Fax: 86-931-8912582

**Abstract**

Separation and recycling of catalysts after catalytic reactions are critically required to reduce the cost of catalysts as well as to avoid the generation of waste in industrial applications. In this paper, ultrafine noble metallic nanoparticles are incorporated into cauliflower-like porous magnetic metal-organic frameworks (MOFs). With the restriction effects of the pore/surface structure in the MOFs, “surfactant-free” metallic nanoparticles are successfully obtained on a 2-3 nm scale. In addition, both the thickness of MOFs shell and the content of noble metallic NPs are tunable on the MOFs coating. Moreover, the microspheres exhibit excellent performance for the catalytic reduction of *p*-nitrophenol with a turnover frequency of 3094 h<sup>-1</sup>. The uniform cavities in the MOFs shell provide docking sites for *p*-nitrophenol and act as confinement nanoreactors, which greatly improve the catalytic performance. Most importantly, the magnetically responsive microspheres can be easily recovered by a magnetic field and show excellent reusability. The as-prepared catalyst also shows good activity for the reduction of other nitrobenzenes. Consequently, this work provides a highly active, magnetically isolable, and recyclable catalyst, which can be used for various catalytic industry processes. The fundamental model can be further employed in a variety of biomedical fields including drug delivery and biological molecules separation.

## 1. Introduction

Noble metallic nanoparticles (NPs) have attracted growing attention owing to their unique physical, chemical, and biological properties and great potential in various fields.<sup>1-7</sup> They are expected to be the suitable candidates for design of highly active and selective catalysts. However, nanoparticles tend to aggregate to form larger particles due to their large surface area, leading to the decrease of their initial activities during the catalytic cycles<sup>8-9</sup>. Therefore, many attempts have been made to immobilize noble metallic NPs on solid supports<sup>9-11</sup>. Among the wide range of supports, magnetic nanomaterials exhibit distinct advantages. Magnetic supports not only enable the catalysts to have magnetic separation property, but also facilitate them to be recycled. Recent examples demonstrate the successful synthesis of metallic NPs on the surface of magnetic substrates.<sup>12-13</sup> However, it is fairly difficult to obtain the metallic NPs on the sub-10 nm scale, especially in the absence of a stabilizer/surfactant<sup>14</sup>. Consequently, the development of producing monodispersed noble metallic NPs on solid supports within several nanometers is highly desirable.

MOFs are crystalline materials composed of metal ions or metal clusters that are connected by organic linkers. They have crystalline structures, large internal surface areas, uniform but tuneable cavities and tailorable chemistry. These distinct characteristics make them very promising for a variety of applications, including gas

56 storage<sup>15-16</sup>, chemical separation<sup>17</sup>, catalysis<sup>18-19</sup>, sensing<sup>20</sup> and drug delivery<sup>21</sup>. In  
57 the context of catalysis, the uses of MOFs as heterogeneous catalysts have recently  
58 received tremendous attention. The nodes of most MOFs are reasonably good Lewis  
59 acid sites, and terminal ligands can present Lewis basic sites. These acid and basic  
60 sites may well function as organic reactions catalysts<sup>22-23</sup>. Recently, by serving as  
61 unique host matrices, the potential applications of MOFs can be extended further by  
62 encapsulating noble metallic (e.g., Pd, Au, Ru, and Pt) or bimetallic alloy NPs within  
63 the frameworks<sup>24</sup>. MOFs limit the growth of NPs in the confined cavities to produce  
64 monodispersed metallic or bimetallic NPs<sup>25-28</sup>. Taking into account the novelty of  
65 MOFs and the recent interest in exploiting their properties as solid catalysts, there is  
66 no doubt that the field of catalysis by embedded NPs in MOFs will continue to attract  
67 much interest in the recent years. However, many unresolved problems still remain a  
68 great challenge. The synthetic procedures require hydrogen and plasma reduction  
69 procedure at high temperature, leading to a high cost and energy wastage. Besides,  
70 efficient separation and recycling of MOFs catalysts after catalytic reactions is  
71 specifically required. Therefore, it is still a challenge to fabricate the type of  
72 multifunctional MOFs materials with a hierarchical structure, which can be applied in  
73 heterogeneous catalysis as well as efficient separation of biological molecules.

74       Herein, we report a facile and efficient method for the fabrication of  
75 magnetically recyclable nanocatalyst with noble metallic NPs encapsulated into  
76 magnetic MOFs. The cauliflower-like microspheres consist of a magnetite core and an

ordered shell of MIL-100(Fe) crystals *via* a layer-by-layer assembly process. Encapsulating the noble metallic NPs within the frameworks was carried out through a simple deposition-reduction method. The whole process is shown in Scheme 1. Compared with other methods of magnetic-Au heterogeneous catalyst formation, no additional toxic reagent is needed. At the same time, both the thickness of MOFs shell and the content of noble metallic NPs are tuneable on the MOFs coating. The synergistic effect between the ultrafine noble metallic NPs (2-3 nm) and MOF shell significantly improved the catalytic performance for the reduction of nitrobenzenes. Moreover, due to the high saturation magnetization and super-paramagnetic property, the as-synthesized nanocatalyst shows high efficiency in magnetic separation and recovery. Thus a magnetically controllable on-off reaction was achieved in the catalytic reduction process. Long-life and high reusability of the as-prepared  $\text{Fe}_3\text{O}_4@\text{M}/\text{MIL-100 (Fe)}$  ( $\text{M}=\text{Au, Pt, Pd}$ ) microspheres are demonstrated without visible decrease in the catalytic performance after several running cycles. These facilitate the practical applications of the catalyst in catalysis.

## 2. Experimental section

### 2.1 Materials

All chemicals were from commercial and used without further purification: mercaptoacetic acid (MAA, Tianjin Chemical Reagent Factory), ferric chloride

97 hexahydrate ( $\text{FeCl}_3 \cdot 6\text{H}_2\text{O}$ , Sinopharm Chemical Reagent Co., Ltd., analytical grade),  
98 1,3,5-benzenetricarboxylic acid ( $\text{H}_3\text{btc}$ , J&K Scientific Ltd., 98%), sodium  
99 borohydride ( $\text{NaBH}_4$ , Sinopharm Chemical Reagent Co., Ltd., 96%), hydrogen  
100 tetrachloroaurate (III) tetrahydrate ( $\text{HAuCl}_4 \cdot 4\text{H}_2\text{O}$ , Shenyang research institute of  
101 nonferrous metals, analytical grade), hydrogen hexachloroplatinate hexahydrate  
102 ( $\text{H}_2\text{PtCl}_6 \cdot 6\text{H}_2\text{O}$ , Shenyang keda reagent factory, analytical grade), palladium chloride  
103 ( $\text{PdCl}_2$ , Shenyang keda reagent factory, analytical grade), *o*-nitrophenol,  
104 *m*-nitrophenol, *p*-nitrophenol, 2,4-dinitrophenol, *o*-nitroaniline, *m*-nitroaniline,  
105 *p*-nitroaniline, 4-Methyl-2-nitroaniline, 4-Methyl-3-nitroaniline and  
106 *p*-Nitrophenylhydrazine (Tianjin Chemical Reagent Factory, analytical grade). A  
107 stock solution of tetrachloropalladinic acid ( $\text{H}_2\text{PdCl}_4$ ) was prepared by dissolving 520  
108 mg of  $\text{PdCl}_2$  into 20 mL of 10% v/v HCl ethanol solution with sonication at room  
109 temperature until complete dissolution.

## 110 2.2 Preparation of magnetic $\text{Fe}_3\text{O}_4$ microspheres

111 The magnetic particles were prepared *via* a solvothermal method<sup>29</sup>. Briefly, 2.70  
112 g of  $\text{FeCl}_3 \cdot 6\text{H}_2\text{O}$  and 7.20 g of sodium acetate were dissolved in 100 mL of ethylene  
113 glycol under vigorous stirring. The resultant homogeneous yellow solution was  
114 transferred to a Teflon-lined stainless-steel autoclave, sealed and heat at 200 °C for 8  
115 h. Then the autoclave was cooled to room temperature. The obtained black magnetite  
116 particles were washed with ethanol for 6 times, and dried in vacuum at 60 °C for 12 h.



### 2.3 Preparation of MAA-functionalized $\text{Fe}_3\text{O}_4$ microspheres

100 mg  $\text{Fe}_3\text{O}_4$  was dispersed in 20 mL of 0.29 mM MAA ethanol solution and stirred for 24 h. The solid products were collected using an external magnetic field and rinsed with ultrapure water and ethanol for three times, then re-dispersed in ethanol for further use.

### 2.4 Preparation of core-shell magnetic $\text{Fe}_3\text{O}_4@\text{MIL-100}$ (Fe) microspheres

$\text{Fe}_3\text{O}_4@\text{MIL-100}$  (Fe) core-shell magnetic microspheres were synthesized according to a previous report of Qiu<sup>30</sup>. Typically, the as-prepared MAA-functionalized  $\text{Fe}_3\text{O}_4$  microspheres were dispersed into the ethanol solution of  $\text{FeCl}_3$  (for 15 min) and  $\text{H}_3\text{btc}$  (for 30 min) separately at 70 °C for a given repeated cycles. Between each step the microspheres were separated with a magnet, and washed with ethanol. Finally the samples were washed with ethanol for three times and dried overnight at 150 °C under vacuum.

### 2.5 Synthesis of magnetic $\text{Fe}_3\text{O}_4@\text{M}/\text{MIL-100}$ (Fe) ( $\text{M}=\text{Au}, \text{Pt}, \text{Pd}$ ) microspheres

Prior to metal loading, the as-synthesized  $\text{Fe}_3\text{O}_4@\text{MIL-100}$  (Fe) microspheres described above were activated by heating at 150 °C for 10 h under dynamic vacuum. Supported noble metallic NPs were prepared *via* a simple deposition-reduction method. Typically, 20 mg of  $\text{Fe}_3\text{O}_4@\text{MIL-100}$  (Fe) powder was dispersed in 2 mL of ethanol and the mixture was sonicated until homogeneous. After stirring for 30 min, ethanol solution of the precursor ( $\text{HAuCl}_4 \cdot 4\text{H}_2\text{O}$ ,  $\text{H}_2\text{PtCl}_6 \cdot 6\text{H}_2\text{O}$  and  $\text{H}_2\text{PdCl}_4$ , 10.00

μmol) was added dropwise with constant vigorous stirring. The resulting solution was continuously stirred for 5 h. Then 500 μL ethanol was added into the slurry followed by adding NaBH<sub>4</sub> (100 mM) ethanol solution under vigorous stirring for the complete reduction of the anionic metal species (700 μL for Fe<sub>3</sub>O<sub>4</sub>@Au/MIL-100 (Fe), 325 μL for Fe<sub>3</sub>O<sub>4</sub>@Pt/MIL-100 (Fe) and 93 μL for Fe<sub>3</sub>O<sub>4</sub>@Pd/MIL-100 (Fe)). After 30 min stirring, the resulting Fe<sub>3</sub>O<sub>4</sub>@M/MIL-100 (Fe) (M=Au, Pt, Pd) microspheres were recovered by a magnet, rinsed with ethanol to remove Cl<sup>-</sup>, and dried under vacuum at 25 °C for 12 h.

## 2.6 Catalytic reduction of aqueous solution of *p*-nitrophenol

Liquid-phase reduction of *p*-nitrophenol to *p*-aminophenol by NaBH<sub>4</sub> was used to characterize the catalytic activity of the Fe<sub>3</sub>O<sub>4</sub>@M/MIL-100 (Fe) (M=Au, Pt, Pd) microspheres. It is a well-known model reaction and has been extensively used to evaluate the catalytic rate of functional composite nanomaterials<sup>31-32</sup>. Typically, 2.75 mL ultrapure water and an aqueous solution (200 μL) of freshly prepared NaBH<sub>4</sub> (100 mM, 20 μmol) were added to a solution (25 μL) of *p*-nitrophenol (10 mM, 0.25 μmol), respectively. Subsequently, 25 μL of aqueous dispersion of the 5.09 wt% Fe<sub>3</sub>O<sub>4</sub>@Au/MIL-100 (Fe) (1.0 mg/mL, 6.46 nmol, Au/*p*-nitrophenol=2.58 mol%), 4.29 wt% Fe<sub>3</sub>O<sub>4</sub>@Pt/MIL-100 (Fe) (1.0 mg/mL, 5.50 nmol, Pt/*p*-nitrophenol=3.65 mol%) or 3.88 wt% Fe<sub>3</sub>O<sub>4</sub>@Pd/MIL-100 (Fe) (1.0 mg/mL, 9.11 nmol, Pd/*p*-nitrophenol=2.58 mol%) catalyst was added to start the reaction. After addition

of the as-synthesized microspheres, the bright yellow solution gradually faded as the reaction proceeded which could be observed by naked eye. The kinetic study of the reaction was performed by measuring the change in the absorbance at 400 nm with time. The absorbance spectra of the solution were measured with a UV-Vis spectrometer in the range 250-550 nm.

The recyclability of the as-prepared catalyst was investigated in the reaction of *p*-nitrophenol reduction. The reduction reaction was amplified twenty times than in previous investigations to facilitate separation and minimize handling errors. After each run, the solid catalyst was recovered using a magnet (complete separation within 30 s), washed with water and ethanol (twice each), dried under vacuum, and reused in the next cycle. The catalytic reduction of other nitrobenzenes was conducted under the same condition of *p*-nitrophenol. The conversions were determined by the gas chromatography/mass spectroscopy (GC/MS) analysis of the residual nitrobenzene in the mixture after reaction.

## 2.7 Characterization

The powder X-ray diffraction (XRD) patterns of the samples were collected on a D/MAX-2000 diffractometer (Rigaku, Japan) using Cu K $\alpha$  radiation (wavelength  $\lambda$ =1.514178 Å) in the  $2\theta$  range 0-80 °. FT-IR spectra were recorded on a Nicolet Nexus 670 fourier transform infrared spectrometer (FT-IR, America) using KBr pellets. Thermogravimetric analysis (TGA) was carried out on a NETZSCH STA 449C

177 thermal analyzer from room temperature to 800 °C at a ramp rate of 10 °C/min in a  
178 flowing 100 mL/min air atmosphere. The morphologies and sizes of the as-prepared  
179 samples were characterized by a Hitachi-600 transmission electron micro-scope  
180 (TEM, Hitachi, Japan) equipped with an energy dispersive X-ray analyzer (EDX) and  
181 a JSM-6701F field emission scanning electron microscope (FE-SEM) at an  
182 accelerating voltage of 15 kV, respectively. Elemental analyses for C/H were  
183 performed on a Perkin-Elmer 2400 Series II analyzer and the species of Fe, Au, Pt  
184 and Pd were analyzed by inductively coupled plasma atomic emission spectrometry  
185 (ICP-AES) (Thermo Jarrel Ash, Franklin, MA, USA). X-ray photoelectron spectra  
186 (XPS) were acquired with a PHI 5702 spectrometer equipped with an Al K $\alpha$  exciting  
187 source. A 2 kV Ar<sup>+</sup> sputter beam was used for depth profiling of Fe<sub>3</sub>O<sub>4</sub>@M/MIL-100  
188 (Fe) (M=Au, Pt, Pd) samples after the initial data were collected. Nitrogen  
189 adsorption-desorption isotherms were obtained at -196 °C on a Quantachrome  
190 AS1Win analyzer. The magnetic behavior was investigated using a vibrating sample  
191 magnetometer (VSM, Lake Shore 7304, Lake Shore, USA) with an applied field  
192 between -15 kOe and 15 kOe at room temperature. The UV-Vis spectra were recorded  
193 on a UV-Vis spectrometer (TU-1901, Beijing, China).

### 194 **3. Results and discussion**

#### 195 *3.1 Structural and Morphological Characterization*

196 The magnetite particles were prepared *via* a robust solvothermal method as  
197 described above. The TEM image shows that the obtained magnetite particles are  
198 uniform with a mean diameter of ~250 nm (Figure 1A). SEM image of the magnetite  
199 particles further confirms the uniform size of ~250 nm and nearly spherical shape  
200 with rough surface (Figure S1A). The surface roughness is attributed to the fact that  
201 the particles are formed by packing many tiny nanocrystals. After 20 assembly cycles  
202 coating with MIL-100 (Fe), core-shell Fe<sub>3</sub>O<sub>4</sub>@MIL-100 (Fe) microspheres with a  
203 MOF layer of about 35 nm in thickness were obtained (Figure 1B). The microspheres  
204 display uniform three-dimensional architecture with cauliflower-like morphology  
205 (Figure 1I). Moreover, with increasing number of assembly cycles, the size of the  
206 whole NPs increases (Figure S1 and Figure 2A-F). In fact, the size of  
207 Fe<sub>3</sub>O<sub>4</sub>@MIL-100 (Fe) microspheres and the thickness of shell shows linear  
208 dependence on the number of assembly cycles (Figure 2G). This suggests that the  
209 thickness of the MOF shell can be rationally controlled by varying the number of  
210 growth cycles using the step-by-step assembly strategy. The subsequent *in situ* growth  
211 process results in a uniform loading of noble metallic NPs (Figure 1C-E). The average  
212 sizes of noble metallic NPs (Figure S2) are about 2.0±0.2 nm (Au NPs), 1.9±0.2 nm  
213 (Pt NPs) and 2.2±0.2 nm (Pd NPs), respectively, which are small enough to be  
214 accommodated in the mesoporous cavities of MIL-100(Fe). However, metallic  
215 particles with bigger sizes were tend to be located on framework surface, as in the  
216 case of metallic NPs loaded into ZIF-8 (diameter of pore window, 11.6 Å), MOF-5

(diameter of pore window, 25.7 Å), and other porous materials<sup>28, 33-35</sup>. In addition, the morphology of the magnetic MOFs microspheres remains unchanged after noble metallic NPs loading (Figure 1J-L). The high-resolution transmission electron microscopy (HRTEM) images show lattice fringes corresponding to an interfringe distance of 0.24 nm (for Au NPs) and 0.23 nm (for Pt and Pd NPs), which can be attributed to the (111) plane of Au<sup>36</sup>, Pt<sup>37</sup> and Pd NPs<sup>38</sup>, respectively (Figure 1F-H). The EDX spectra of the microspheres (Figure S3) also show the presence of Fe and Au/Pt/Pd. In addition, the C, H, Fe and M ratios of the Fe<sub>3</sub>O<sub>4</sub>@M/MIL-100 (Fe) (M=Au, Pt, Pd) microspheres were obtained by elemental analysis and ICP-AES, and the values were listed in Table 1.

To further verify the formation of the Fe<sub>3</sub>O<sub>4</sub>@M/MIL-100 (Fe) (M=Au, Pt, Pd) microspheres, the XRD patterns of Fe<sub>3</sub>O<sub>4</sub>, Fe<sub>3</sub>O<sub>4</sub>@MIL-100 (Fe) and Fe<sub>3</sub>O<sub>4</sub>@M/MIL-100 (Fe) (M=Au, Pt, Pd) samples were carried out, as shown in Figure 3. The diffraction peaks in curve a can be indexed to the face-centred cubic lattice of Fe<sub>3</sub>O<sub>4</sub> nanospheres according to JCPDS 75-1609<sup>39</sup>. After coating with the MOF layer, the diffraction pattern of the resulting material (curve b) shows some new diffraction peaks (labeled with the symbol ★) in addition to the Fe<sub>3</sub>O<sub>4</sub> reflections, demonstrating the formation of the crystal MIL-100 (Fe)<sup>30</sup>. The sharp and strong peaks at 2-4° reveal the presence of both micropores and mesopores<sup>40</sup>. After the *in situ* growth process, there is no loss of crystallinity in the XRD patterns for the

resultant  $\text{Fe}_3\text{O}_4@\text{M}/\text{MIL-100}$  (Fe) (M=Au, Pt, Pd) microspheres (curves c, d and e).

Compared with the simulated pattern of MIL-100 (Fe) (curve f), we conclude that the integrity of the MIL-100 (Fe) framework is maintained. The weak diffraction reflections of typical cubic Au NPs<sup>36</sup> (curves c), face-centred Pt NPs<sup>41</sup> (curve d) and Pd NPs<sup>38</sup> (curve e) are also detected, indicating the formation of very small M NPs (M=Au, Pt, Pd), which matches well with the TEM observations. No diffraction peaks from any other impurities are detected. The XRD results indicate that the metal precursors are successfully reduced to metallic NPs.

Figure 4A shows the FT-IR spectrum of  $\text{Fe}_3\text{O}_4$ ,  $\text{Fe}_3\text{O}_4@\text{MIL-100}$  (Fe), and  $\text{Fe}_3\text{O}_4@\text{M}/\text{MIL-100}$  (Fe) (M=Au, Pt, Pd) nanocomposites. The band at 590 and 636  $\text{cm}^{-1}$  are assigned to Fe-O and C-S stretching vibrations of MAA-functionalized  $\text{Fe}_3\text{O}_4$ , respectively. The peaks at 1435 and 1575  $\text{cm}^{-1}$  are owing to the stretching vibrations of C=C in benzene ring, while the peaks at 1376 and 1618  $\text{cm}^{-1}$  are attributed to C=O stretching vibrations of carboxylic acid, suggesting that MIL-100 (Fe) shell has been successfully coated on the surface of  $\text{Fe}_3\text{O}_4$ . In addition, FT-IR and TGA analyses (Figure 4B) show that the as-synthesized microspheres have similar peaks or curves to  $\text{Fe}_3\text{O}_4@\text{MIL-100}$  (Fe), indicating the retention of the MIL-100 (Fe) framework and the absence of new bond/structure. The results are in good agreement with that obtained from XRD pattern.

The BET surface area measurements were performed with  $N_2$  adsorption/desorption isotherms at  $-196\text{ }^\circ\text{C}$ . Before measurements, all the samples were evacuated at  $150\text{ }^\circ\text{C}$  for 12 h. The pore volume was calculated by a single point method at  $P/P_0=0.992$ . As determined by  $N_2$  sorption isotherms (Figure 5), the BET surface areas of  $\text{Fe}_3\text{O}_4@\text{MIL-100 (Fe)}$ ,  $\text{Fe}_3\text{O}_4@\text{M/MIL-100 (Fe)}$  ( $\text{M}=\text{Au, Pt, Pd}$ ) microspheres are 319, 211, 173 and  $186\text{ m}^2/\text{g}$ , respectively. And their pore volumes are 0.45, 0.41, 0.39 and  $0.40\text{ cm}^3/\text{g}$ , respectively. Furthermore, estimation of the pore size distribution by the density functional theory (DFT) shows two maxima at 1.5 and 2.2 nm for  $\text{Fe}_3\text{O}_4@\text{MIL-100 (Fe)}$ , which is consistent with the previously reported data<sup>42</sup>. The pore sizes are big enough for the metallic precursors to diffuse into the pores (the diameters of the metallic precursors ( $\text{AuCl}_4^-$ ,  $\text{PtCl}_6^{2-}$ , and  $\text{PdCl}_4^{2-}$ ) were calculated by Chemdraw to be 3.8 Å, 4.6 Å, and 4.2 Å, respectively). The nucleation can take place within it to form the noble metallic NPs. As compared with  $\text{Fe}_3\text{O}_4@\text{MIL-100 (Fe)}$ , the surface areas and the pore volumes of  $\text{Fe}_3\text{O}_4@\text{M/MIL-100 (Fe)}$  ( $\text{M}=\text{Au, Pt, Pd}$ ) are appreciably decreased. The results indicate that the pores of the host frameworks are occupied by dispersed M NPs ( $\text{M}=\text{Au, Pt, Pd}$ ) and/or blocked by the M NPs located on framework surface, as in the case of M NPs loaded into ZIF-8, MOF-5, and other porous materials<sup>28, 33-35</sup>.

The magnetic properties of the resultant multifunctional microspheres were investigated at room temperature by VSM in the field range from  $-20$  to  $+20\text{ kOe}$ , as



shown in Figure 6. They exhibit super-paramagnetic behaviour, little hysteresis, remanence and coercivity due to the fact that the particles are composed of ultrafine magnetite nanocrystals. A reduction of magnetization saturation ( $M_s$ ) value is observed for  $\text{Fe}_3\text{O}_4@\text{MIL-100}$  (Fe) microspheres after growing assembly cycles (Figure S4). This could be attributed to the decrease in the density of  $\text{Fe}_3\text{O}_4$ , which is corresponding to the increase of outer-layer thickness as shown in SEM (Figure S1) and TEM (Figure 2). After loading with Au, Pt and Pd NPs, the  $M_s$  values of  $\text{Fe}_3\text{O}_4@\text{M}/\text{MIL-100}$  (Fe) (M=Au, Pt, Pd) are slightly decreased to 44.47, 43.90 and 45.07 emu/g, respectively (Figure 6A). It should be noted that the microspheres can be dispersed in water by sonication or vigorous shaking, resulting in a brown-coloured suspension. One can observe fast aggregation of the microspheres from their homogeneous dispersion in the presence of an external magnetic field, and quick redispersion with a slight shaking once the magnetic field is removed (Figure 6B). These results directly demonstrate the excellent magnetic responsivity and redispersibility, which is important in terms of their practical manipulation.

In order to further demonstrate the composition details of the resulting hybrid magnetic microspheres, XPS was performed. The sensitivity of XPS in chemical analysis stems mostly from its ability to resolve the chemical identity of the atoms from the measured binding energies. Figure 7A exhibits the overall surveys of the as-synthesized  $\text{Fe}_3\text{O}_4@\text{M}/\text{MIL-100}$  (Fe) (M=Au, Pt, Pd) microspheres, which clearly

shows the signals of C, O and Fe elements. Well-defined peaks corresponding to metallic Au, Pt and Pd species can also be detected (Figure 7B-D). The position of the Au 4f, Pt 4f and Pd 3d peaks are corresponding to Au<sup>0</sup>, Pt<sup>0</sup> and Pd<sup>0</sup>, respectively, which are in good agreement with the previous literature <sup>43-44</sup>. From these spectra, it can be observed that all the metal ions (Au<sup>3+</sup>, Pt<sup>4+</sup> and Pd<sup>2+</sup>) impregnated in Fe<sub>3</sub>O<sub>4</sub>@MIL-100 (Fe) are reduced to noble metallic NPs after the *in situ* growth process by NaBH<sub>4</sub> reduction.

### 3.2 Application in catalytic reduction of *p*-nitrophenol

In this investigation, the catalytic performance of Fe<sub>3</sub>O<sub>4</sub>@M/MIL-100 (Fe) (M=Au, Pt, Pd) microspheres for efficient reduction of *p*-nitrophenol to *p*-aminophenol has been intensively investigated <sup>32, 45</sup>. *P*-nitrophenol aqueous solution exhibits a distinct spectral profile with an absorption maximum at 317 nm. After the addition of NaBH<sub>4</sub>, a red-shift of the absorption peak to 400 nm is observed (Figure 8A). A colour change from light yellow to bright yellow indicates the formation of *p*-nitrophenolate <sup>46</sup>. Moreover, there is little change for the maximum absorption at 400 nm over time even after adding excess NaBH<sub>4</sub> solution, confirming that the reduction couldn't proceed without catalyst. As a comparison, the catalytic ability of an equal amount of Fe<sub>3</sub>O<sub>4</sub> and Fe<sub>3</sub>O<sub>4</sub>@MIL-100 (Fe) is also studied. As shown in Figure 8B, there is little change in absorbance at 400 nm within 30 min over Fe<sub>3</sub>O<sub>4</sub> and Fe<sub>3</sub>O<sub>4</sub>@MIL-100 (Fe), while complete reduction of *p*-nitrophenol is achieved

within a short time over the as-synthesized catalysts. Superior catalytic performance of the  $\text{Fe}_3\text{O}_4@\text{M}/\text{MIL}-100$  (Fe) (M=Au, Pt, Pd) catalysts confirm that the applied magnetic MOFs can serve as an excellent support for noble metallic NPs.

Figure 9A-C unambiguously exhibit the time-dependent UV-Vis absorption spectra for a typical reduction process using  $\text{Fe}_3\text{O}_4@\text{M}/\text{MIL}-100$  (Fe) (M=Au, Pt, Pd) microspheres as catalysts. After addition of the catalyst, the absorption intensity at 400 nm significantly decreases and the characteristic absorption of *p*-aminophenol appears at 300 nm. The appearance of this new peak was verified by superimposing the UV-Vis spectrum of pure *p*-aminophenol under identical conditions (Figure 8A, d). The formation of *p*-aminophenol was further confirmed from gas chromatography-mass (GC-MS) analytic technique (Figure S5). As can be seen from Figure S5, after the reduction reaction, the characteristic peak of *p*-nitrophenol (Figure S5A, M-1: 138.06) disappeared, accompanied by the appearance of characteristic peak of *p*-aminophenol (Figure S5B, M+1: 110.06). The data provide a supportive evidence for the efficient reduction of *p*-nitrophenol to *p*-aminophenol. The UV-Vis spectra show an isosbestic point at 313 nm (Figure 8A), illustrating that the catalytic reduction of *p*-nitrophenol yields *p*-aminophenol only, without by-product<sup>32</sup>. Considering that the concentration of  $\text{NaBH}_4$  is much higher than that of *p*-nitrophenol ( $C_{\text{NaBH}_4}/C_{p\text{-nitrophenol}}=80$ ) in the reaction system, a pseudo first-order kinetic equation with regard to *p*-nitrophenol only can be applied to evaluate the

catalytic rate<sup>47</sup>. The kinetic equation for the reduction reaction of *p*-nitrophenol can be expressed as  $\ln (C_t/C_0) = -K_{app}t$ , where  $K_{app}$  is the kinetic rate constant,  $C_0$  is the initial concentration of *p*-nitrophenol, and  $C_t$  is the concentration of *p*-nitrophenol at time  $t$ . Linear relationships between  $\ln (C_t/C_0)$  and reaction time are displayed in Figure 9D, which match well with the first-order reaction kinetics. The kinetic rate constant  $K_{app}$  is calculated to be  $2.58 \text{ min}^{-1}$  for  $\text{Fe}_3\text{O}_4@\text{Pt}/\text{MIL-100 (Fe)}$  (Figure S6), which is superior to other noble metallic-based catalysts<sup>33, 48-49</sup>. This means that the nanocomposites show excellent catalytic activity for the reduction of *p*-nitrophenol.

The catalytic activity of the as-synthesized  $\text{Fe}_3\text{O}_4@\text{Pt}/\text{MIL-100 (Fe)}$  catalyst for the reduction of other nitrobenzene analogs including nitrophenol, nitroaniline and nitrophenylhydrazine were also investigated (Table 2). Figure S9 clearly shows the typical changes of UV-Vis absorption spectra of these nitrobenzene compounds during the reduction processes, demonstrating that the reduction of these nitrobenzenes indeed occur in the presence of a small amount of catalyst. Additionally, as shown in Table 2, the catalyst exhibits good catalytic activity (high TOF values) with excellent yields toward a series of nitrobenzene compounds regardless of the types and position of the substituents (the turnover frequency (TOF) is defined as moles (or numbers) of the product molecules generated per moles (or numbers) of catalyst surface atoms per hour<sup>12</sup>). Moreover, the catalysts  $\text{Fe}_3\text{O}_4@\text{Au}/\text{MIL-100 (Fe)}$  and  $\text{Fe}_3\text{O}_4@\text{Pd}/\text{MIL-100 (Fe)}$  also show high catalytic activity toward the reduction

of these nitrobenzene compounds, as illustrated in Table S2 and Table S3. These results indicate the generality and the efficacy of the new catalysts toward the reduction of the series of nitrobenzenes.

It will be significant to compare the catalytic performance of  $\text{Fe}_3\text{O}_4@\text{M}/\text{MIL}-100$  (Fe) (M=Au, Pt, Pd) with previous reported analogous catalysts. As shown in Table 3, the TOF value can reach  $3094 \text{ h}^{-1}$  for  $\text{Fe}_3\text{O}_4@\text{Pt}/\text{MIL}-100$  (Fe), which is significantly higher than those reported in previous studies<sup>49-53</sup>. From Table 3 we can conclude that the as-synthesized catalysts in the present work have a higher catalytic activity than those of most other catalysts. Thus, a simple and efficient preparation of a  $\text{Fe}_3\text{O}_4@\text{M}/\text{MIL}-100$  (Fe) (M=Au, Pt, Pd) catalyst with high catalytic efficiency was presented in our work.

It should be pointed out that the catalytic performance of the as-prepared  $\text{Fe}_3\text{O}_4@\text{M}/\text{MIL}-100$  (Fe) (M=Au, Pt, Pd) microspheres with different assembly cycles are also studied (Figure S7). Although more Pt NPs are embedded in the porous as the MOF shell grows (Figure S8), the percentages of the elements in MIL-100(Fe) (C, H and Fe) increase significantly, leading to a decrease of the metallic content (Table S1). Based on the relative changes in the contents of the C, H, Fe, Pt observed in Table S1 and the corresponding different catalytic performance, we conclude that the intensities of the noble metallic NPs plays a key role in the catalysis.

In addition to catalytic activity, the stability is a very important property for the reusability of catalysts. Recyclability of the as-prepared catalyst is tested. The catalytic activity remains stable even after running for 10 cycles for  $\text{Fe}_3\text{O}_4@\text{M}/\text{MIL}-100$  (Fe) (M= Pt, Pd) and the conversion of each cycle remains nearly 100%. After reused for 8 cycles, the catalyst  $\text{Fe}_3\text{O}_4@\text{Au}/\text{MIL}-100$  (Fe) gradually loses its catalytic activity. However, the conversion of upon 85% is maintained (Figure 10). The high stability can be attributed to the core-shell porous architecture of the as-prepared microspheres, which provides both docking sites for *p*-nitrophenol (the MOF shell) and a super-paramagnetic core allowing easy manipulation by a magnet. In addition, there's no change for adsorption spectra of the solutions after given reduction cycles (Figure S10), which further confirms the long-term stability of the catalysts. Leaching test with the catalyst  $\text{Fe}_3\text{O}_4@\text{Pt}/\text{MIL}-100$  (Fe) was also carried out under reaction conditions. The solid catalyst was magnetically separated from the reactant mixture after each catalytic cycle. The residual solution was collected and measured by ICP-AES to determine the lost amount of Pt and Fe. No Fe element was found in the residual solution, suggesting that the  $\text{Fe}_3\text{O}_4$  NPs were well protected by the MOFs shell. Besides, only trace amount of Pt element was detected in the residual solution. As shown in Figure S11, nearly 80% of Pt content was maintained on the catalyst even after 10 runs, which proved the good stability of the catalyst. Together with the high recyclability of the catalyst (Figure 10), these results clearly demonstrate the stability of the noble metallic NPs in  $\text{Fe}_3\text{O}_4@\text{MIL}-100$  (Fe).

396 The interactions between noble metallic NPs and the support directly affect the  
397 catalytic activity of the catalyst, which could mostly explain the different catalytic  
398 activities of noble metallic NPs in different reports. In this work, a magnetic MOF  
399 was used as support for Au, Pt and Pd NPs with superior catalytic activity. Scheme 2  
400 depicts the performance of the  $\text{Fe}_3\text{O}_4@\text{M}/\text{MIL}-100$  (Fe) (M=Au, Pt, Pd) microspheres  
401 as catalysts in the reduction of *p*-nitrophenol to *p*-aminophenol by  $\text{NaBH}_4$ . Possible  
402 mechanism of excellent catalytic activity may be explained as follows: given that  
403 *p*-nitrophenol is  $\pi$ -rich in nature, it is expected that *p*-nitrophenol can be adsorbed  
404 onto the porous MOFs shell by means of  $\pi$ - $\pi$  stacking interactions between the  
405 aromatic rings of *p*-nitrophenol and the organic units of the framework, and  
406 coordination effects between phenolic hydroxy of *p*-nitrophenol and metal center of  
407 the framework<sup>48, 54</sup>. The mesoporous of MOFs serve as millions of nanoreactors,  
408 where the reduction actions take place *via* relaying electrons from the donor  $\text{BH}_4^-$  to  
409 the acceptor *p*-nitrophenol. In aqueous medium  $\text{BH}_4^-$  is adsorbed onto the surface of  
410 catalyst. The hydrogen atom, which is formed from the hydride, after electron transfer  
411 to the noble metallic NPs, attacks *p*-nitrophenol molecules to reduce it<sup>55</sup>. The  
412 adsorption over the porous MOFs shell provides a high concentration of *p*-nitrophenol  
413 near to the noble metallic NPs embedded in the MOFs cavities, leading to highly  
414 efficient contact between them. Thus enhancement of the catalytic efficiency for  
415 *p*-nitrophenol reduction is achieved. It is worthwhile to note that more experimental

or theoretical evidences are still needed to get the exact mechanism of the enhanced activity.

#### 4. Conclusions

In summary, we have developed an environmentally friendly method to prepare cauliflower-like magnetic  $\text{Fe}_3\text{O}_4@\text{M}/\text{MIL-100}(\text{Fe})$  ( $\text{M}=\text{Au}, \text{Pt}, \text{Pd}$ ) microspheres and investigated their superior catalytic properties in the effective reduction of nitrobenzenes compounds. The microspheres show unique structural features such as magnetic core, porous MOFs shell and monodispersed small noble metallic NPs. The contents of noble metallic NPs and the thickness of MOFs shell can be easily controlled by varying the assembly cycles on MOFs coating. The magnetic MOFs support not only enhances the catalytic activity, but lends the catalyst easiness of separation and recovery. The  $\text{Fe}_3\text{O}_4@\text{M}/\text{MIL-100}(\text{Fe})$  ( $\text{M}=\text{Au}, \text{Pt}, \text{Pd}$ ) microspheres maintain high catalytic activity over several reduction cycles. Therefore, this functional nanostructure holds great promise as novel noble metallic-based catalysts for various catalytic reactions. Additionally, the fundamental concept for the multifunctional magnetic MOFs can be extended to the fabrication of multicomponent nanosystem with integrated and enhanced properties for various advanced applications, such as chemical/biosensor, biological molecule separation, drug delivery, and so on.



436 **Acknowledgements**

437 This work was supported by the National Natural Science Foundation of China  
438 (Nos. 21375053, 21207057).

439

## References

1. J. N. Anker, W. P. Hall, O. Lyandres, N. C. Shah, J. Zhao and R. P. Van Duyne, *Nat. Mater.*, 2008, **7**, 442.
2. C. Langhammer, E. M. Larsson, B. Kasemo and I. Zorić, *Nano Lett.*, 2010, **10**, 3529.
3. J. Huang, T. Jiang, H. Gao, B. Han, Z. Liu, W. Wu, Y. Chang and G. Zhao, *Angew. Chem. Int. Ed.*, 2004, **116**, 1421.
4. A. O. Govorov and H. H. Richardson, *Nano Today*, 2007, **2**, 30.
5. B. D. Chithrani, A. A. Ghazani and W. C. W. Chan, *Nano Lett.*, 2006, **6**, 662.
6. T. K. Sau, A. L. Rogach, F. Jäckel, T. A. Klar and J. Feldmann, *Adv. Mater.*, 2010, **22**, 1805.
7. T. S. Hauck, A. A. Ghazani and W. C. W. Chan, *Small*, 2008, **4**, 153.
8. M. Zhu, Y. Wang, C. Wang, W. Li and G. Diao, *Catal. Sci. Technol.*, 2013, **3**, 952.
9. C. Zhu, L. Han, P. Hu and S. Dong, *Nanoscale*, 2012, **4**, 1641.
10. Z. Sun, B. Sun, M. Qiao, J. Wei, Q. Yue, C. Wang, Y. Deng, S. Kaliaguine and D. Zhao, *J. Am. Chem. Soc.*, 2012, **134**, 17653.
11. T. Yu, J. Zeng, B. Lim and Y. Xia, *Adv. Mater.*, 2010, **22**, 5188.
12. Q. M. Kainz, R. Linhardt, R. N. Grass, G. Vilé, J. Pérez - Ramírez, W. J. Stark and O. Reiser, *Adv. Funct. Mater.*, doi: 10.1002/adfm.201303277.

- 460 13. R. Linhardt, Q. M. Kainz, R. N. Grass, W. J. Stark and O. Reiser, *RSC Advances*,  
461 2014, **4**, 8541.
- 462 14. Y.-T. Kim, H. Lee, H.-J. Kim and T.-H. Lim, *Chem. Commun.*, 2010, **46**, 2085.
- 463 15. N. L. Rosi, J. Eckert, M. Eddaoudi, D. T. Vodak, J. Kim, M. O'Keeffe and O. M.  
464 Yaghi, *Science*, 2003, **300**, 1127.
- 465 16. O. K. Farha, A. Özgür Yazaydın, I. Eryazici, C. D. Malliakas, B. G. Hauser, M.  
466 G. Kanatzidis, S. T. Nguyen, R. Q. Snurr and J. T. Hupp, *Nat. Chem.*, 2010, **2**,  
467 944.
- 468 17. Y. Hu, Z. Huang, J. Liao and G. Li, *Anal. Chem.*, 2013, **85**, 6885.
- 469 18. J. Hermannsdörfer, M. Friedrich, N. Miyajima, R. Q. Albuquerque, S. Kümmel  
470 and R. Kempe, *Angew. Chem. Int. Ed.*, 2012, **51**, 11473.
- 471 19. T. Toyao, M. Saito, Y. Horiuchi, K. Mochizuki, M. Iwata, H. Higashimura and  
472 M. Matsuoka, *Catal. Sci. Technol.*, 2013.
- 473 20. C.-X. Yang, H.-B. Ren and X.-P. Yan, *Anal. Chem.*, 2013, **85**, 7441.
- 474 21. P. Horcajada, T. Chalati, C. Serre, B. Gillet, C. Sebrie, T. Baati, J. F. Eubank, D.  
475 Heurtaux, P. Clayette, C. Kreuz, J.-S. Chang, Y. K. Hwang, V. Marsaud, P.-N.  
476 Bories, L. Cynober, S. Gil, G. Ferey, P. Couvreur and R. Gref, *Nat. Mater.*, 2010,  
477 **9**, 172.
- 478 22. A. Dhakshinamoorthy, M. Opanasenko, J. Čejka and H. Garcia, *Adv. Synth.*  
479 *Catal.*, 2013, **355**, 247.

- 480 23. A. Dhakshinamoorthy, M. Opanasenko, J. Čejka and H. Garcia, *Catal. Sci.*  
481 *Technol.*, 2013, 3, 2509.
- 482 24. V. Pascanu, Q. Yao, A. Bermejo Gómez, M. Gustafsson, Y. Yun, W. Wan, L.  
483 Samain, X. Zou and B. Martín - Matute, *Chemistry-A European Journal*, 2013,  
484 **19**, 17483.
- 485 25. H. Liu, Y. Li, H. Jiang, C. Vargas and R. Luque, *Chem. Commun.*, 2012, **48**,  
486 8431.
- 487 26. G. Chen, S. Wu, H. Liu, H. Jiang and Y. Li, *Green Chem.*, 2013, **15**, 230.
- 488 27. H. R. Moon, D.-W. Lim and M. P. Suh, *Chem. Soc. Rev.*, 2013, **42**, 1807.
- 489 28. Q.-L. Zhu, J. Li and Q. Xu, *J. Am. Chem. Soc.*, 2013, **135**, 10210.
- 490 29. Y. Deng, D. Qi, C. Deng, X. Zhang and D. Zhao, *J. Am. Chem. Soc.*, 2007, **130**,  
491 28.
- 492 30. F. Ke, L.-G. Qiu, Y.-P. Yuan, X. Jiang and J.-F. Zhu, *J. Mater. Chem.*, 2012, **22**,  
493 9497.
- 494 31. Y. Fang and E. Wang, *Nanoscale*, 2013, **5**, 1843.
- 495 32. Y. Deng, Y. Cai, Z. Sun, J. Liu, C. Liu, J. Wei, W. Li, C. Liu, Y. Wang and D.  
496 Zhao, *J. Am. Chem. Soc.*, 2010, **132**, 8466.
- 497 33. H.-L. Jiang, T. Akita, T. Ishida, M. Haruta and Q. Xu, *J. Am. Chem. Soc.*, 2011,  
498 **133**, 1304.

- 499 34. Y. K. Hwang, D.-Y. Hong, J.-S. Chang, S. H. Jhung, Y.-K. Seo, J. Kim, A.  
500 Vimont, M. Daturi, C. Serre and G. Férey, *Angew. Chem. Int. Ed.*, 2008, **47**,  
501 4144.
- 502 35. Y. E. Cheon and M. P. Suh, *Angew. Chem. Int. Ed.*, 2009, **48**, 2899.
- 503 36. J. Zheng, Y. Dong, W. Wang, Y. Ma, J. Hu, X. Chen and X. Chen, *Nanoscale*,  
504 2013, **5**, 4894.
- 505 37. S. Lin, C. Shen, D. Lu, C. Wang and H.-J. Gao, *Carbon*, 2013, **53**, 112.
- 506 38. T. Yao, T. Cui, X. Fang, F. Cui and J. Wu, *Nanoscale*, 2013, **5**, 5896.
- 507 39. H. Deng, X. Li, Q. Peng, X. Wang, J. Chen and Y. Li, *Angew. Chem. Int. Ed.*,  
508 2005, **117**, 2842.
- 509 40. G. Férey, C. Mellot-Draznieks, C. Serre, F. Millange, J. Dutour, S. Surblé and I.  
510 Margiolaki, *Science*, 2005, **309**, 2040.
- 511 41. V.-D. Dao and H.-S. Choi, *Chem. Commun.*, 2013, **49**, 8910.
- 512 42. R. Canioni, C. Roch-Marchal, F. Secheresse, P. Horcajada, C. Serre, M.  
513 Hardi-Dan, G. Férey, J.-M. Greneche, F. Lefebvre, J.-S. Chang, Y.-K. Hwang, O.  
514 Lebedev, S. Turner and G. Van Tendeloo, *J. Mater. Chem.*, 2011, **21**, 1226.
- 515 43. X. Liu, S. Ye, H.-Q. Li, Y.-M. Liu, Y. Cao and K.-N. Fan, *Catal. Sci. Technol.*,  
516 2013, **3**, 3200.
- 517 44. X. Gu, Z.-H. Lu, H.-L. Jiang, T. Akita and Q. Xu, *J. Am. Chem. Soc.*, 2011, **133**,  
518 11822.

- 519 45. Y. Lu, Y. Mei, M. Drechsler and M. Ballauff, *Angew. Chem. Int. Ed.*, 2006, **45**,  
520 813.
- 521 46. J.-M. Song, S.-S. Zhang and S.-H. Yu, *Small*, doi: 10.1002/smll.201301386.
- 522 47. Y. Mei, Y. Lu, F. Polzer, M. Ballauff and M. Drechsler, *Chem. Mater.*, 2007, **19**,  
523 1062.
- 524 48. F. Ke, J. Zhu, L.-G. Qiu and X. Jiang, *Chem. Commun.*, 2013, **49**, 1267.
- 525 49. W. Hu, B. Liu, Q. Wang, Y. Liu, Y. Liu, P. Jing, S. Yu, L. Liu and J. Zhang,  
526 *Chem. Commun.*, 2013, **49**, 7596.
- 527 50. B. Liu, S. Yu, Q. Wang, W. Hu, P. Jing, Y. Liu, W. Jia, Y. Liu, L. Liu and J.  
528 Zhang, *Chem. Commun.*, 2013, **49**, 3757.
- 529 51. X. Wang, D. Liu, S. Song and H. Zhang, *J. Am. Chem. Soc.*, 2013, **135**, 15864.
- 530 52. E. Lam, S. Hrapovic, E. Majid, J. H. Chong and J. H. T. Luong, *Nanoscale*, 2012,  
531 **4**, 997.
- 532 53. X. Wu, C. Lu, W. Zhang, G. Yuan, R. Xiong and X. Zhang, *J. Mater. Chem. A*,  
533 2013, **1**, 8645.
- 534 54. F. Millange, C. Serre, N. Guillou, G. Férey and R. I. Walton, *Angew. Chem. Int.*  
535 *Ed.*, 2008, **47**, 4100.
- 536 55. J.-P. Deng, W.-C. Shih and C.-Y. Mou, *J. Phys. Chem. C*, 2007, **111**, 9723.
- 537

538

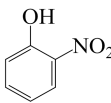
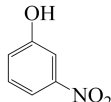
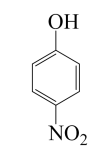
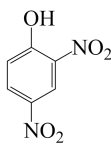
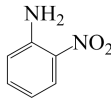
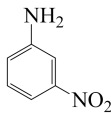
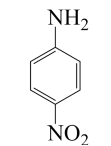
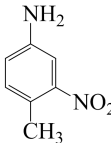
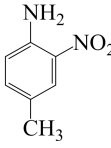
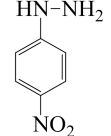
539 **Table 1.** Elemental and ICP analyses for the samples with 20 assembly cycles.

Sample	Found (%)
Fe <sub>3</sub> O <sub>4</sub> @Au/MIL-100 (Fe)	C, 9.33; H, 1.554; Fe, 44.34; Au, 5.09
Fe <sub>3</sub> O <sub>4</sub> @Pt/MIL-100 (Fe)	C, 10.06; H, 1.386; Fe, 43.99; Pt, 4.29
Fe <sub>3</sub> O <sub>4</sub> @Pd/MIL-100 (Fe)	C, 9.23; H, 1.488; Fe, 44.23; Pd, 3.88

540

541

**Table 2** Reduction of various nitrobenzenes using Fe<sub>3</sub>O<sub>4</sub>@Pt/MIL-100 (Fe) catalyst<sup>a</sup>

Entry	Compound	Structure	Time/s	Conversion (%)	TOF (h <sup>-1</sup> )
1	<i>o</i> -Nitrophenol		50	90.8	2973
2	<i>m</i> -Nitrophenol		45	98.2	3573
3	<i>p</i> -Nitrophenol		50	94.5	3094
4	2,4-Dinitrophenol		450	93.4	340
5	<i>o</i> -Nitroaniline		100	95.3	1560
6	<i>m</i> -Nitroaniline		75	95.8	2091
7	<i>p</i> -Nitroaniline		120	95.1	1297
8	4-Methyl-3-nitroaniline		100	91	1490
9	4-Methyl-2-nitroaniline		180	92.7	843
10	<i>p</i> -Nitrophenylhydrazine		270	92.8	563

<sup>a</sup> Reaction condition: 25  $\mu$ L of 10 mM nitrobenzene, 25  $\mu$ L of 1.0 mg/mL catalyst, and 200  $\mu$ L of 100 mM fresh NaBH<sub>4</sub>.



**Table 3.** Comparison of various catalysts for the reduction of *p*-nitrophenol.

Catalyst	Au/Pt/Pd content (wt. %)	Size of Au/Pt/Pd (nm)	TOF (h <sup>-1</sup> )	Ref.
Fe <sub>3</sub> O <sub>4</sub> @TiO <sub>2</sub> /Au@Pd@TiO <sub>2</sub>	0.69 (Au), 0.17 (Pd)	5	891	40
@Au/CeO <sub>2</sub>	2.97	3~5	240	41
@Pd/CeO <sub>2</sub>	0.18		1068	
Pt@CeO <sub>2</sub> /RGO	- <sup>a</sup>	3~5	90	42
Au/PDDA/NCC	1.45	2.95 ± 0.06	212	43
Pd/CNs	1.06	1–40	880	44
Fe <sub>3</sub> O <sub>4</sub> @Au/MIL-100 (Fe)	5.09	2~3	223	This work
Fe <sub>3</sub> O <sub>4</sub> @Pt/MIL-100 (Fe)	4.29	2~3	3094	This work
Fe <sub>3</sub> O <sub>4</sub> @Pd/MIL-100 (Fe)	3.88	2~3	1343	This work

<sup>a</sup> No data presented.

**Figure captions**

**Figure 1.** TEM and SEM images of (A)  $\text{Fe}_3\text{O}_4$  particles, (B, I)  $\text{Fe}_3\text{O}_4@\text{MIL-100}$  (Fe), (C, J)  $\text{Fe}_3\text{O}_4@\text{Au/MIL-100}$  (Fe), (D, K)  $\text{Fe}_3\text{O}_4@\text{Pt/MIL-100}$  (Fe) and (E, L)  $\text{Fe}_3\text{O}_4@\text{Pd/MIL-100}$  (Fe) microspheres with 20 assembly cycles. (F-H) HRTEM images of the Au, Pt and Pd NPs, respectively. Inset is the SAED pattern recorded on a single particle.

**Figure 2.** TEM images of individual (A)  $\text{Fe}_3\text{O}_4$  and  $\text{Fe}_3\text{O}_4@\text{MIL-100}$  (Fe) core-shell nanospheres after (B) 15, (C) 20, (D) 30, (E) 40, and (F) 60 assembly cycles. (G) The correlations between the assembly cycles and the resulting diameter (red line) and shell thickness (black line), obtained from the TEM investigations by averaging over 50 NPs.

**Figure 3.** XRD patterns of (a)  $\text{Fe}_3\text{O}_4$ , (b)  $\text{Fe}_3\text{O}_4@\text{MIL-100}$  (Fe), (c)  $\text{Fe}_3\text{O}_4@\text{Au/MIL-100}$  (Fe), (d)  $\text{Fe}_3\text{O}_4@\text{Pt/MIL-100}$  (Fe), (e)  $\text{Fe}_3\text{O}_4@\text{Pd/MIL-100}$  (Fe) after 20 assembly cycles, (f) MIL-100 (Fe) (simulated). • represents  $\text{Fe}_3\text{O}_4$  nanospheres; ★ represents MIL-100 (Fe); ■ represents Au NPs; ▼ represents Pt NPs; ♦ represents Pd NPs.

568

569 **Figure 4.** (A) FT-IR spectra of (a)  $\text{Fe}_3\text{O}_4$ , (b)  $\text{Fe}_3\text{O}_4@\text{MIL-100 (Fe)}$  microspheres and  
570  $\text{Fe}_3\text{O}_4@\text{MIL-100 (Fe)}$  microspheres with 20 assembly cycles after embedded with (c)  
571 Au, (d) Pt, (e) Pd NPs; (B) TGA analyses under air of  $\text{Fe}_3\text{O}_4@\text{MIL-100 (Fe)}$   
572 microspheres with 20 assembly cycles before (a) and after embedded with (b) Au, (c)  
573 Pt, (d) Pd NPs.

574

575 **Figure 5.** (A) Nitrogen sorption isotherms at  $-196^\circ\text{C}$  and (B) pore size distribution  
576 curves for the as-synthesized (a)  $\text{Fe}_3\text{O}_4@\text{MIL-100 (Fe)}$ , (b)  $\text{Fe}_3\text{O}_4@\text{Au/MIL-100 (Fe)}$ ,  
577 (c)  $\text{Fe}_3\text{O}_4@\text{Pt/MIL-100 (Fe)}$  and (d)  $\text{Fe}_3\text{O}_4@\text{Pd/MIL-100 (Fe)}$  with 20 assembly  
578 cycles.

579

580 **Figure 6.** (A) Room-temperature magnetic hysteresis loops of (a)  $\text{Fe}_3\text{O}_4$ , (b)  
581  $\text{Fe}_3\text{O}_4@\text{MIL-100 (Fe)}$ , (c)  $\text{Fe}_3\text{O}_4@\text{Au/MIL-100 (Fe)}$ , (d)  $\text{Fe}_3\text{O}_4@\text{Pt/MIL-100 (Fe)}$   
582 and (e)  $\text{Fe}_3\text{O}_4@\text{Pd/MIL-100 (Fe)}$  with 20 assembly cycles. (B) Magnetic  
583 separation–redispersion process of  $\text{Fe}_3\text{O}_4@\text{Pt/MIL-100 (Fe)}$  microspheres with 20  
584 assembly cycles.

585

**Figure 7.** (A) Survey XPS spectra of  $\text{Fe}_3\text{O}_4@\text{M}/\text{MIL-100}$  (Fe) (M=Au, Pt, Pd) with 20 assembly cycles. (B) High-resolution Au 4f XPS spectrum of  $\text{Fe}_3\text{O}_4@\text{Au}/\text{MIL-100}$  (Fe). (C) High-resolution Pt 4f XPS spectrum of  $\text{Fe}_3\text{O}_4@\text{Pt}/\text{MIL-100}$  (Fe). (D) High-resolution Pd 3d XPS spectrum of  $\text{Fe}_3\text{O}_4@\text{Pd}/\text{MIL-100}$  (Fe).

**Figure 8.** (A) UV-Vis absorption spectra of *p*-nitrophenol before (a) and after (b) adding  $\text{NaBH}_4$  solution, (c) UV-Vis spectrum of the resultant reduction solution with the catalyst, (d) UV-Vis spectrum of pure *p*-aminophenol. Inset: photograph of *p*-nitrophenol with (1) and without (2)  $\text{NaBH}_4$  addition; (B)  $C_t/C_0$  versus reaction time for the reduction of *p*-nitrophenol with (a)  $\text{Fe}_3\text{O}_4$ , (b)  $\text{Fe}_3\text{O}_4@\text{MIL-100}$  (Fe), (c)  $\text{Fe}_3\text{O}_4@\text{Au}/\text{MIL-100}$  (Fe), (d)  $\text{Fe}_3\text{O}_4@\text{Pt}/\text{MIL-100}$  (Fe) and (e)  $\text{Fe}_3\text{O}_4@\text{Pd}/\text{MIL-100}$  (Fe) microspheres with 20 assembly cycles.

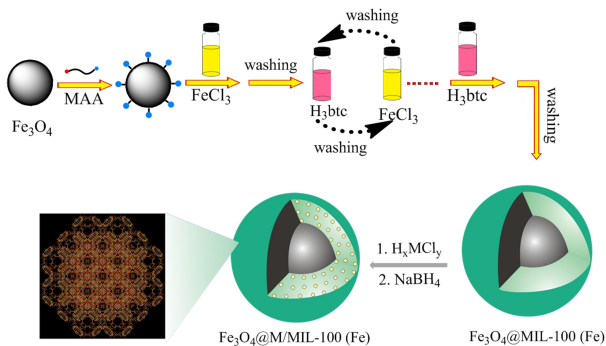
**Figure 9.** Time dependent absorption spectra for the catalytic reduction of *p*-nitrophenol by  $\text{NaBH}_4$  in presence of 25  $\mu\text{g}$  catalyst: (A)  $\text{Fe}_3\text{O}_4@\text{Au}/\text{MIL-100}$  (Fe), (B)  $\text{Fe}_3\text{O}_4@\text{Pt}/\text{MIL-100}$  (Fe), (C)  $\text{Fe}_3\text{O}_4@\text{Pd}/\text{MIL-100}$  (Fe) with 20 assembly cycles. (D) The relationships of  $\ln(C_t/C_0)$  versus reaction time plot in presence of 25  $\mu\text{g}$  different catalysts: (a) No catalysts, (b)  $\text{Fe}_3\text{O}_4@\text{MIL-100}$  (Fe), (c)  $\text{Fe}_3\text{O}_4@\text{Au}/\text{MIL-100}$  (Fe), (d)  $\text{Fe}_3\text{O}_4@\text{Pd}/\text{MIL-100}$  (Fe), and (e)  $\text{Fe}_3\text{O}_4@\text{Pt}/\text{MIL-100}$

(Fe) with 20 assembly cycles. Conditions: [*p*-nitrophenol] = 0.083 mM; [NaBH<sub>4</sub>] = 6.67 mM, 25 °C.

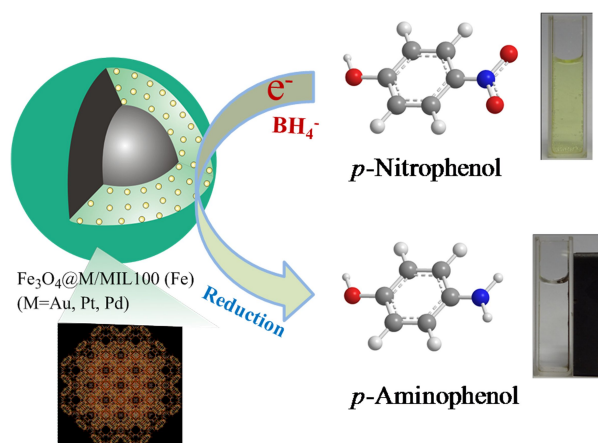
607

**Figure 10.** The reusability of the as-prepared catalysts for the reduction of *p*-nitrophenol with NaBH<sub>4</sub>: (a) Fe<sub>3</sub>O<sub>4</sub>@Au/MIL-100 (Fe), (b) Fe<sub>3</sub>O<sub>4</sub>@Pt/MIL-100 (Fe), and (c) Fe<sub>3</sub>O<sub>4</sub>@Pd/MIL-100 (Fe) with 20 assembly cycles.

611

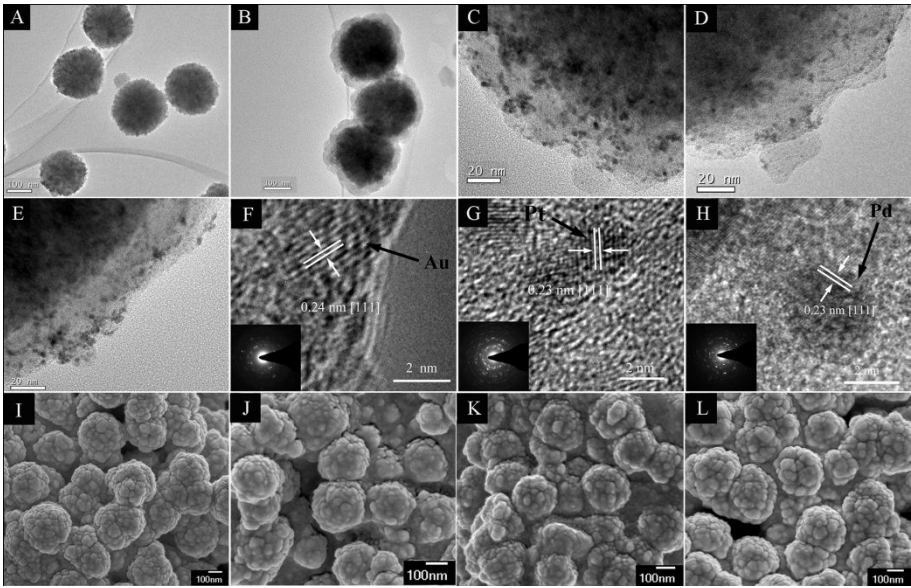


**Scheme 1.** Schematic illustration of fabrication of Fe<sub>3</sub>O<sub>4</sub>@M/MIL-100 (Fe) (M=Au, Pt, Pd) microspheres. MAA: Mercaptoacetic acid; H<sub>3</sub>btc: 1,3,5-benzenetricarboxylic acid.

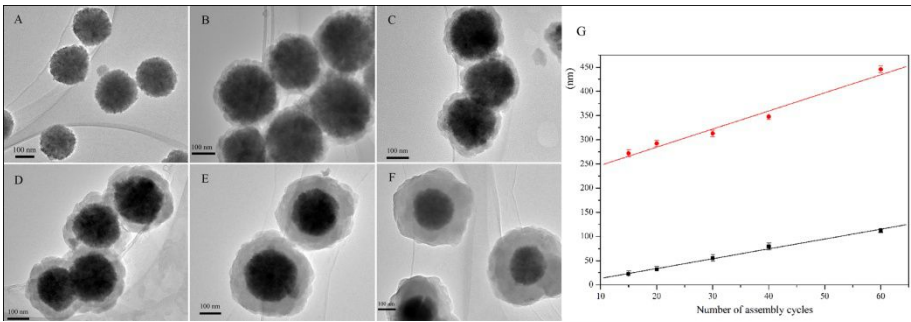


**Scheme 2.** Schematic and photographic representation of the performance of  $\text{Fe}_3\text{O}_4@\text{M}/\text{MIL}-100$  (Fe) (M=Au, Pt, Pd) microspheres as catalysts for the reduction of *p*-nitrophenol.

**Figure 1**



**Figure 2**





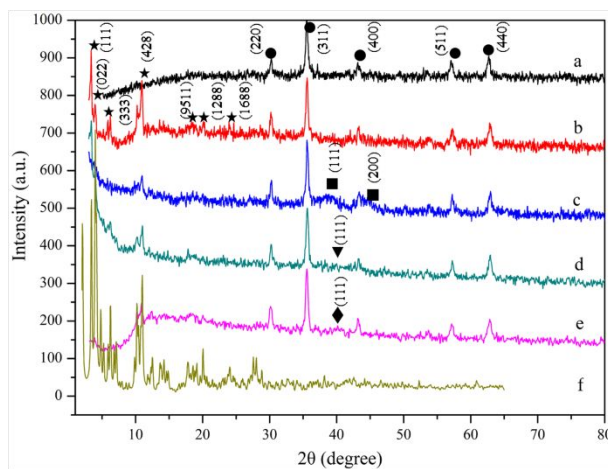
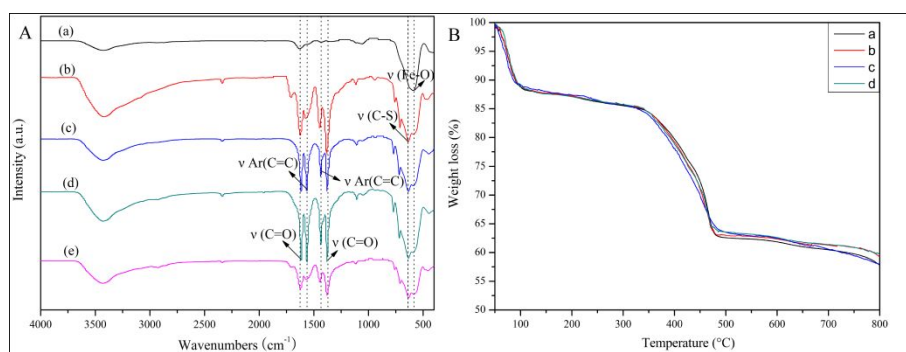
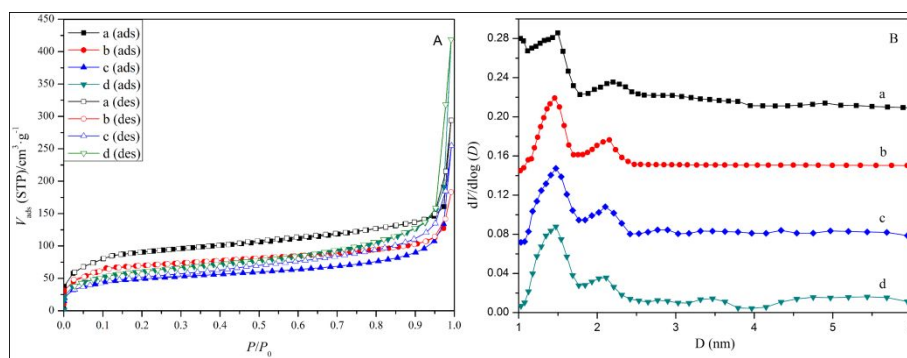
628 **Figure 3**630 **Figure 4**634 **Figure 5**

Figure 6

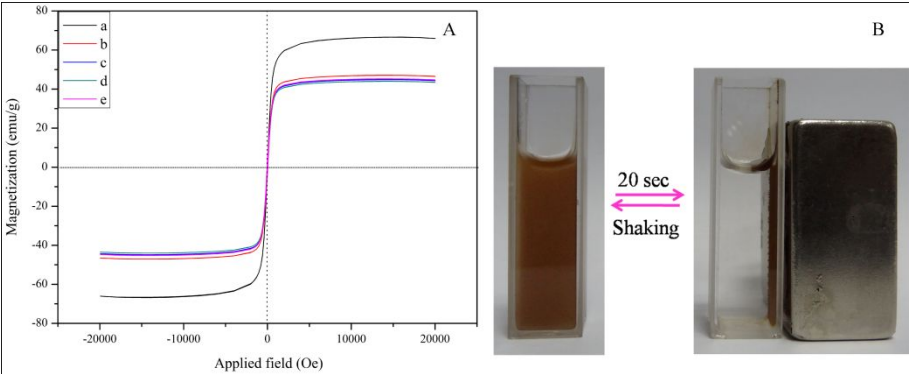
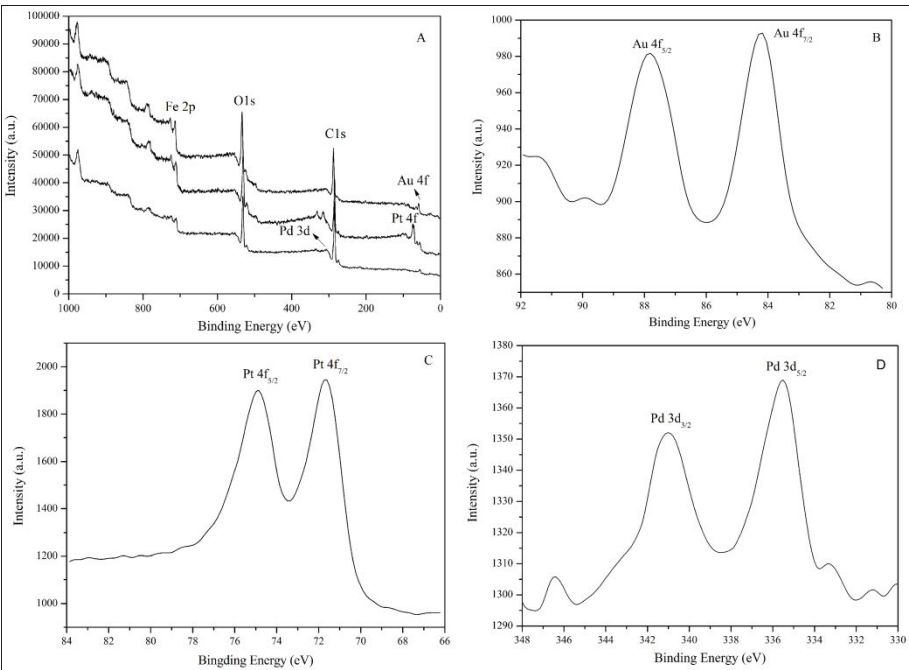


Figure 7



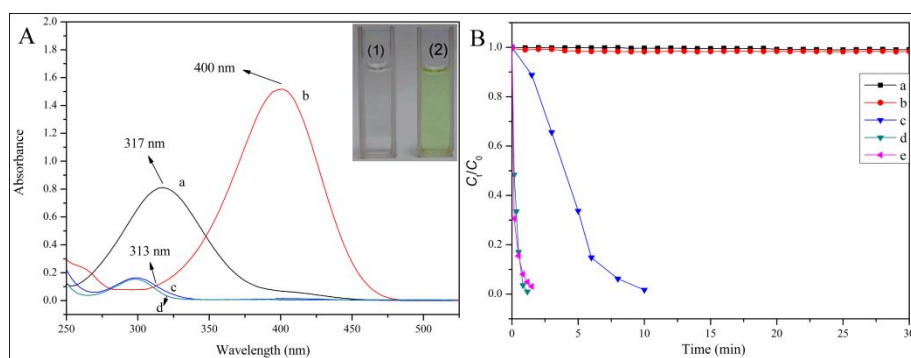
**Figure 8**

Figure 9

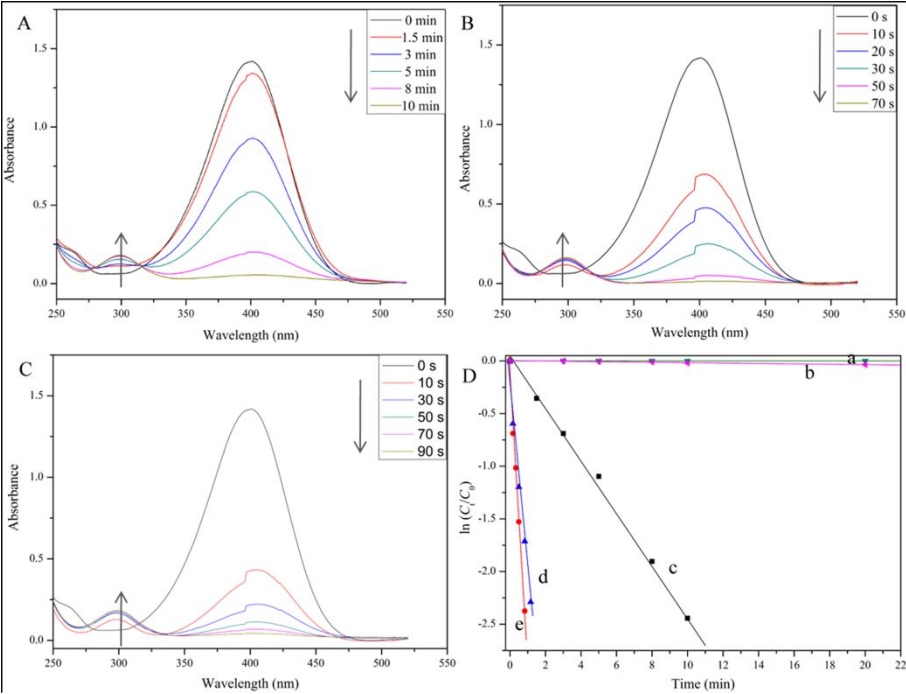


Figure 10

